# Journal of Materials Chemistry A

Accepted Manuscript






ROYAL SOCIETY OF CHEMISTRY

www.rsc.org/materialsA

# Vertically Stacked Bilayer $CuCo_2O_4/MnCo_2O_4$ Heterostructures on Functionalized Graphite Paper for High-Performance Electrochemical Capacitors

Shude Liu[a], Kwan San Hui[b,*], Kwun Nam Hui[c,*], Je Moon Yun[d], Kwang Ho Kim[a, d*]

[a]Department of Materials Science and Engineering, Pusan National University, San 30 Jangjeon-dong, Geumjeong-gu, Busan 609-735, Republic of Korea.

[b]Department of Mechanical Convergence Engineering, Hanyang University, 17 Haengdang-dong, Seongdong-gu, Seoul 133-791, Republic of Korea.

[c]Institute of Applied Physics and Materials Engineering, University of Macau, Avenida da Universidade, Taipa, Macau, China.

[d]Global Frontier R&D Center for Hybrid Interface Materials, Pusan National University, 30 Jangjeon-dong, Geumjung-gu, Busan 609-735, Republic of Korea.

[*]*Corresponding author:*

*E-mail:* kshui@hanyang.ac.kr *(Kwan San Hui)*

*Tel: +82 2-2220-0441; Fax: +82 2-2220-2299*

*E-mail:* bizhui@umac.mo *(Kwun Nam Hui)*

*Tel: +853 8822-4426; Fax: +853 8822-2426*

*E-mail:* kwhokim@pusan.ac.kr *(Kwang Ho Kim)*

**Abstract**

Cobaltite system with spinel structures is a promising cathode material for next-generation high-performance electrochemical capacitor because of its high stability in electrochemistry. However, increasing the mass loading of active materials without sacrificing the geometry of the nanostructures remains a challenge. In this study, we propose vertically stacked bilayer spinel heterostructures constructed from hierarchical $CuCo_2O_4/MnCo_2O_4$ on graphite paper as highly capable supercapacitor electrode. A two-step hydrothermal method with post annealing treatment is used in the preparation of heterostructures. $CuCo_2O_4/MnCo_2O_4$ electrode delivers remarkable specific capacitance of 1434 F $g^{-1}$ at 0.5 A $g^{-1}$, considerable high-rate capability (810 F $g^{-1}$ at 15 A $g^{-1}$), and an excellent cycling stability maintaining 81.4% at 10 A $g^{-1}$ after 5000 cycles. An electrochemical capacitor device operating at 1.6 V is constructed using $CuCo_2O_4/MnCo_2O_4$ and graphene as positive and negative electrodes, respectively. The device shows high energy density of 42.1 Wh $kg^{-1}$ at a power density of 400 W $kg^{-1}$, as well as good cycling stability (88.4% retention after 10000 cycles). The stacking concept of heteronanostructures can potentially enrich the electrochemical performance of metal oxides for next-generation electrochemical capacitors.

## Introduction

The continuous increase in energy demand has significantly stimulated a considerable number of studies for energy storage and conversion applications.[1, 2] Electrochemical capacitors have attracted extensive attention because of their overall advantages of bridging the gap between batteries and conventional capacitors.[3-5] However, most commercial supercapacitors still suffer from low energy density (3–5 Wh $kg^{-1}$), high cost, and bulky issues in certain consumer products, such as laptops, electronic digital cameras, and mobile phones.[5, 6] Therefore, developing an advanced electrochemical capacitor with advantages of high energy density, lightweight, and low cost while maintaining intrinsic high power density and long cycle life is imperative.

Among the reported metal oxides, spinel ($A_xB_{3-x}O_4$, where A and B are two different transition metals of Co, Mn, Ni, Fe, and Zn types) demonstrates high redox reactions and improves electronic conductivity, which are generally beneficial to electrochemical applications.[6-8] Binary spinel cobaltites, such as $CuCo_2O_4$,[7] $NiCo_2O_4$,[4] $ZnCo_2O_4$,[8] and $MnCo_2O_4$,[6] have been generally studied as high-capacity anodes for lithium–ion batteries and as cathode electrode materials for electrochemical capacitors with an enhanced energy and power densities. Nevertheless, cobalt-based spinel materials can easily suffer from decreasing capacity and low conductivity.[9] Consequently, doping approach has been reported to improve the cycling performance of cobalt-based spinel materials because of enhanced electrical conductivity and richer electroactive elements in the doped metal oxides.[10] However, high dose of dopants is difficult to realize in spinel materials because the Fermi level is often pinned in a narrow energy region in the gap and would not shift much when more dopants are added;[11] moreover, high dose of doping will inevitably degrade the structural properties of spinel host.

Recently, heterostructures electrode materials have proven to be an effective strategy for utilizing electroactive materials in achieving high-performance energy storage devices, such as supercapacitors[12, 13] and lithium-ion batteries[14, 15] due to the following advantages: (1) heterostructures provides more active sites for desirable electron transport pathways at the materials surface; (2) the open-network and free interspaces among heterostructures can be efficiently utilized, which shorten ion diffusion paths and improve the utilization rate of electrode materials;[16] (3) the synergistic combination of the virtues of the individual components resulting in richer Faradaic redox reactions. On the other hand, electrode with large mass loading is also a critical prerequisite for high energy density electrochemical capacitor. The loading mass of metal oxide on mesoporous Ni foam is generally less than 1 mg $cm^{-2}$ via a single-step hydrothermal process.[17] Hence, multistep hydrothermal processes were reported to increase the mass loading of electrode. For example, Yang et al. reported an ultrathin $Co_3O_4$ nanosheet supercapacitors with reasonable mass loading delivering high energy density that reaches 134 Wh $kg^{-1}$ at a high power density of 111 W $kg^{-1}$ at 5 mA $cm^{-2}$ via a two-step hydrothermal process.[18] Similarly, Luan et al. reported an electrochemical capacitor that consists of NiO nanoflake and reduced graphene oxide (rGO) as cathode and anode, respectively; this capacitor has a maximum energy density of 39.9 W h $kg^{-1}$ by repeating the hydrothermal treatment to increase the mass loading of rGO sheets on the nickel foam anode electrode.[19]

Direct integration of electroactive materials on graphitic electrode materials, such as MOF-derived carbon,[20] carbon nanotube,[21] and graphene[22, 23] have demonstrated to improve the life cycle and good rate capability of supercapacitor devices substantially[24] by reducing the resistivity imposed on the electrodes because of the use of polymer binder between electroactive

materials and current collector.[4] Notably, graphite paper is the most promising current collector because of its high conductivity and inherent advantages, such as lightweight, bendable, inert under ambient conditions, and low cost.[13] In addition, functionalized graphite paper can provide large functional groups for anchoring electroactive materials during synthesis.[7, 13] Thus, graphite paper is a promising binder-free substrate for energy storage devices.

To address the above challenges of obtaining high-performance electrode materials combining high mass loading, multiple distinct electrochemical signatures, and binder-free electrode approach, a rational design of vertically stacked bilayer spinel heterostructures is proposed. These heterostructures are constructed from microflower-like $MnCo_2O_4$ grown on top of $CuCo_2O_4$ that is initially grown on graphite paper ($CuCo_2O_4/MnCo_2O_4$) as high-rate capability supercapacitor electrode via a two-step hydrothermal method with post annealing treatment. As-prepared $CuCo_2O_4/MnCo_2O_4$ electrode exhibits high specific capacitance of 1434 F $g^{-1}$ at a current density of 0.5 A $g^{-1}$, considerable high rate capability (810 F $g^{-1}$ at 15 A $g^{-1}$), and excellent cycling stability maintaining 81.4% at 10 A $g^{-1}$ after 5000 cycles when evaluated as electrode for electrochemical capacitor. An electrochemical capacitor device that operates at 1.6 V is constructed using $CuCo_2O_4/MnCo_2O_4$ and graphene as positive and negative electrodes, respectively. The device shows high energy density of 42.1 Wh $kg^{-1}$ at a power density of 400 W $kg^{-1}$, as well as good cycling stability (88.4% retention after 10000 cycles).

## Experimental

*Preparation of Functionalized Graphite Paper*

All reagents were of analytical grade and used as received. The graphite paper was cleaned several times with acetone, ethanol, and deionized water, and dried at room temperature. Subsequently, the graphite paper was functionalized through an electrochemical treatment to increase the number of oxygen functional groups. A typical three-electrode configuration measurement was conducted, with graphite paper, Pt, and $Hg/Hg_2Cl_2$ saturated calomel electrode (SCE) as the working, counter, and reference electrodes, respectively. An aqueous solution that contained 1 M $H_2SO_4$ was used as the electrolyte at 2.2 V for 20 min. Subsequently, the samples were cleaned several times with deionized water and then dried at 120 °C in a vacuum oven.

*Synthesis of Vertically Stacked $CuCo_2O_4/MnCo_2O_4$ Heterostructures*

All chemicals were used as received. Typically, 2 mmol of $Co(NO_3)_2{\cdot}6H_2O$ and 1 mmol of $Cu(NO_3)_2{\cdot}3H_2O$ were dissolved into 40 mL of deionized water and ethanol (volume ratio = 1:1) to form a homogeneous pink solution. Urea (12 mmol) was added to the homogeneous solution through magnetic stirring, and the reaction solution was transferred to a 50 mL Teflon-lined stainless steel autoclave. The clean graphite paper substrate with 2.0 cm × 5.0 cm size was immersed into the reaction solution. Subsequently, the autoclave was heated to 120 °C for 8 h and then cooled naturally to room temperature. The graphite paper loaded with a precursor was washed several times with distilled water and ethanol, and dried in an oven at 60 °C for 12 h to yield the CuCo precursor on the graphite paper (detailed information in Fig. S1).

The synthesized $(Cu,Co)_2(CO_3)(OH)_2$ was used as the scaffold for the growth of $MnCo_2O_4$ active materials. $(Cu,Co)_2(CO_3)(OH)_2$ anchored on the graphite paper was placed into a 50 mL Teflon-lined stainless steel autoclave that contained a homogeneous solution of 2 mmol of $Co(NO_3)_2{\cdot}6H_2O$, 1 mmol of $Mn(NO_3)_2{\cdot}6H_2O$, 12 mmol of urea, and 40 mL of deionized water and ethanol (volume ratio = 1:1) for the two-step hydrothermal growth of MnCo precursor. Afterward, the autoclave was heated to 120 °C for 8 h and then cooled naturally to room temperature. The graphite paper loaded with a precursor was washed several times with distilled water and ethanol, and dried in an oven to yield the bilayer CuCo/MnCo-precursor heterostructures on the graphite paper. The final product was obtained by annealing the precursor at 350 °C for 3 h in air. For comparison, $CuCo_2O_4$ nanosheets grown on graphite paper were synthesized under the same conditions without the addition of $Co(NO_3)_2{\cdot}6H_2O$ and $Mn(NO_3)_2{\cdot}6H_2O$. The mass loadings of the bilayer $CuCo_2O_4/MnCo_2O_4$ and $CuCo_2O_4$ on the graphite paper were approximately 1.41 and 0.86 mg $cm^{-2}$, respectively.

*Characterization of Materials*

The microstructure and morphology of the as-obtained samples were characterized by scanning electron microscopy (SEM; Hitachi, S-4800) equipped with energy dispersive spectroscopy (EDS) and high-resolution transmission electron microscopy (HRTEM; JEOL 2100F). The cross section of the samples were characterized by focus ion beam (FIB; Carl Zeiss, Crossbeam 540) equipped with EDS (Oxford Instruments, X-Max$^N$ 20). The crystallographic structure of the samples was tested by X-ray diffraction (XRD; D8-Discovery Bruker, 40 kV, 40 mA, Cu Kα, λ = 1.5406 Å), and the functional groups on the samples were examined by Fourier transform infrared absorption spectroscopy (FTIR; VERTEX70). X-ray photoelectron spectroscopy (XPS;

VG Scientifics ESCALAB250) was performed to analyze the chemical bonding status of the material. The XPS spectra of the $CuCo_2O_4$ powder were obtained after the sonication of the graphite paper; these spectra were calibrated to the C 1s peak at 284.6 eV. Micromeritics 3Flex was used to measure the pore structures using nitrogen sorption under 77 K. The pore size distribution was calculated Barrett-Joyner-Halenda (BJH) method. The mass was weighted by a semi-micro balance (Precisa, XR205SM-DR) with a readability of 0.01 mg.

*Electrochemical Characterization*

The electrochemical performances of the samples (1 × 1 $cm^2$) were evaluated in a traditional three-electrode electrolytic cell by cyclic voltammetry (CV) at various scan rates that ranged from 2 mV $s^{-1}$ to 20 mV $s^{-1}$ at a potential window of −0.2 V to 0.6 V. A galvanostatic charge–discharge test was also performed in a 2.0 M KOH electrolyte within the range of 0–0.6 V versus SCE at various current densities. The electrochemical impedance spectroscopy (EIS) measurement was conducted over a frequency range of 100 kHz–0.01 Hz at the open circuit potential with AC potential amplitude of 5 mV. All electrochemical experiments were conducted using a three-electrode mode multichannel electrochemical workstation (nSTAT, IVIUM Technologies). The specific capacitance ($C_s$) was calculated using equation 1: [25]

$$Cs = \frac{I \times t}{\Delta V \times m} \tag{1}$$

where $I$ (mA) is the constant discharge current, $t$ (s) is the discharge time, $\Delta V$ (V) is the voltage drop upon discharging (excluding the IR drop), and $m$ (mg) is the mass of the active materials.

*Fabrication of $CuCo_2O_4/MnCo_2O_4$//graphene/Ni Foam Hybrid Device*

For the assembly of $CuCo_2O_4/MnCo_2O_4$//graphene/Ni foam (NF) device, a graphene/NF working electrode was first prepared by mixing commercial graphene (Fig. S2), acetylene black, and poly(tetrafluoroethylene) suspension (60 wt.%) binder at a weight ratio of 80:10:10. The slurry was directly coated on a porous nickel foam and dried overnight in a vacuum oven at 60 °C. Based on the three-electrode electrochemical measurement results of both $CuCo_2O_4/MnCo_2O_4$ and graphene electrodes, cell balance was achieved by setting the electrode mass ratio of cathode/anode to 0.24 (the anode loading mass is around 5.92 mg $cm^{-2}$) (Fig. S3). The graphene/NF electrode was pressed and combined with a $CuCo_2O_4/MnCo_2O_4$ electrode using a piece of cellulose paper (and 2.0 M KOH as the separator and electrolyte, respectively, to assemble the full cell. The specific capacitance ($C_{device}$), energy density ($E$), and power density ($P$) were calculated according to the following equations 2-4:[26]

$$C_{device} = \frac{I \times \Delta t}{\Delta V \times M} \quad (2)$$

$$E = \frac{1}{2} C_{device} \Delta V^2 \quad (3)$$

$$P = E / \Delta t \quad (4)$$

where $I$ is the discharge current, $\Delta t$ is the discharge time, $M$ is the total mass of both positive and negative electrodes, and $\Delta V$ is the potential window of the device.

**Results and Discussion**

The facile method used for the fabrication of vertically stacked bilayer $CuCo_2O_4/MnCo_2O_4$ heterostructures on functionalized graphite paper is schematically illustrated in Fig. 1a. First,

graphite paper is functionalized with oxygen-containing functional groups, such as carbonyl, hydroxyl, and carboxylic groups, according to our previous study.[13] FTIR spectrum was carried out to investigate the functional groups present on the surface of the functionalized graphite paper. Fig. S4 shows FTIR spectra of the functionalized and pristine graphite papers. The observed intense peak at 1059 $cm^{-1}$ can be assigned to C–O (alkoxy functional group) stretching vibration,[27] while the peak appeared at 1232 $cm^{-1}$, corresponds to the C–OH (epoxy functional group) stretching vibration.[28] The absorption peaks at 1564 and 1634 $cm^{-1}$ are related to the skeletal vibrations of C=C (aromatics functional group) from unoxidized graphitic domains.[27] Moreover, the peaks at 1683 and 1749 $cm^{-1}$ display the characteristic band for C = O stretch of carboxylic acid group.[28, 29] In addtion, two adsorbing peaks at 2847 and 2917 $cm^{-1}$ are related to C–H vibration from alkyl chain.[27, 30] These results clearly demonstated that the graphite paper was functionalized with various oxygen functional groups by electrochemical treatment. Second, flower-like $(Cu,Co)_2(CO_3)(OH)_2$ (Fig. S5 (a,b)) that consists of porous nanosheets is uniformly grown on graphite paper via a preferred orientation growth process.[31] Fig. S5 (c,d) show the EDX data of $(Cu,Co)_2(CO_3)(OH)_2$ on graphite paper, thereby confirming the existence of Cu, Co, O, and C elements in the prepared samples. In the hydrothermal process, the slow hydrolysis of urea results in the in situ release of $OH^-$ and $CO_3^{2-}$, which further initiates the precipitation of $Cu^{2+}$ and $Co^{2+}$ to form CuCo-based carbonate hydroxide species.[24] The first step in the precursor generation is the formation of amorphous *M* salts, where *M* presents $Cu^{3+}$ or $Co^{2+}$, on the graphite paper. The nascent precursors attached to the graphite paper function as the nucleation sites. As the freshly formed nanonuclei are thermodynamically unstable because of the high surface energy, they tend to gather together to minimize the interfacial energy, thus resulting in the aggregation of supersaturated nuclei.[31] As the reaction proceeds, the concentration of the

reactants becomes lower, and new particles are continuously grown along the oriented direction on the initially formed precursor aggregations. Consequently, small nanosheets form and further grow along the specific directions to interlace and overlap with one another into a network structure; this structure constitutes the flower-like morphology. The chemical reaction mechanism can be expressed in equations (5-6):[32, 33]

$$2NH_2(CO)NH_2 + 5H_2O \rightarrow 4NH_4^+ + 2OH^- + CO_3^{2-} + CO_2 \quad (5)$$

$$(Cu^{2+}, Co^{2+}) + 2OH^- + CO_3^{2-} \rightarrow (Cu,Co)_2(CO_3)(OH)_2 \quad (6)$$

Finally, the sphere-like $MnCo_2O_4$ precursor composed of ultrathin nanosheets is anchored onto the surface of the $CuCo_2O_4$ precursor via a similar preferred orientation growth process through a second hydrothermal process. During the reaction, $(Cu,Co)_2(CO_3)(OH)_2$ nanosheets are used as "substrates," which provide the platform for the growth of $MnCo_2O_4$ without stabilizers and surfactant. Vertically stacked CuCo/MnCo precursor (Fig. S6) is calcined in air, and $CuCo_2O_4/MnCo_2O_4$ with well-retained nanosheets morphology is thereby obtained. Finally, the flower-like CuCo/MnCo precursor species can be converted into $CuCo_2O_4/MnCo_2O_4$ heterostructures through the following simple oxidation reactions:

$$Cu_2(CO_3)(OH)_2 + 2Co_2(CO_3)(OH)_2 + O_2 \rightarrow 2CuCo_2O_4 + 3CO_2 + 3H_2O \quad (7)$$

$$Mn_2(CO_3)(OH)_2 + 2Co_2(CO_3)(OH)_2 + O_2 \rightarrow 2MnCo_2O_4 + 3CO_2 + 3H_2O \quad (8)$$

Fig. 1b reveals the crystal structure of the microsphere flower-like $CuCo_2O_4$ and vertically stacked $CuCo_2O_4/MnCo_2O_4$ heterostructures. The diffraction peaks of $CuCo_2O_4$ microsphere at $2\theta$ values of 19.18°, 31.41°, 37.05°, 59.63°, and 65.83° can be well identified as (111), (220), (311), (511), and (440) planes of the spinel $CuCo_2O_4$ phase (JCPDS 01-1155). The XRD pattern of as-synthesized $MnCo_2O_4$ is also shown. Diffraction peaks at about 18.71°, 30.75°, 36.21°,

44.11°, and 64.23° can be indexed to (111), (220), (311), (400), and (440) phases of $MnCo_2O_4$ (JCPDS 01-1130). All the major diffraction peaks of $CuCo_2O_4$ and $MnCo_2O_4$ can also be identified in the patterns of $CuCo_2O_4/MnCo_2O_4$ heterostructures; no extra peak is detected, thus suggesting the high purity of the products. Based on the Scherrer equation:[34]

$$\tau = \frac{k\lambda}{\beta \cos\theta} \tag{9}$$

where $\tau$ is the mean size of the ordered (crystalline) domains, $k$ is a dimensionless shape factor, $\lambda$ is the X-ray wavelength, $\beta$ is the line broadening at half the maximum intensity (FWHM), and $\theta$ is the Bragg angle. The average crystalline sizes of $CuCo_2O_4$, $MnCo_2O_4$ and $CuCo_2O_4/MnCo_2O_4$ were calculated to be 2.43, 2.49 and 2.50 nm, respectively.

FTIR spectroscopy is performed to examine the molecular structural changes and confirm the formation of $CuCo_2O_4/MnCo_2O_4$ heterostructures after annealing. Fig. 1c shows the FTIR spectra of $CuCo_2O_4/MnCo_2O_4$ precursor and $CuCo_2O_4/MnCo_2O_4$ samples. The peaks at approximately 3406 $cm^{-1}$ correspond to the –OH stretching band, and the peak at 1517 $cm^{-1}$ indicates the existence of the bending modes of absorbed water molecules.[35] Furthermore, the peaks at approximately 1382 and 1045 $cm^{-1}$ are assigned to the stretching vibrations of $\nu OCO_2$.[35] The spectra clearly show the characteristic in-plane and out-of-plane bending vibrations of $CO_3^{2-}$ at 874 and 748 $cm^{-1}$.[36] Other absorption bands below 700 $cm^{-1}$ are associated with metal–oxygen stretching and bending modes in the $CuCo_2O_4/MnCo_2O_4$ precursor. Based on the above analysis, the precursor can be identified as a typical copper cobalt hydroxide carbonate compound (both $CO_3^{2-}$ and $OH^-$ anions derived from urea acted as precipitants).[37] After annealing treatment, two extremely strong peaks centered at 660 and 556 $cm^{-1}$ are observed, which confirms the presence of spinel $CuCo_2O_4/MnCo_2O_4$ heterostructures.[38]

The elemental composition and oxidation state of $CuCo_2O_4/MnCo_2O_4$ heterostructures are characterized by XPS. The Gaussian fitting results show that the Cu 2p emission spectrum (Fig. 2a) presents two main peaks; Cu 2p peaks are also fitted with two main peaks at binding energies of 934.4 and 954.2 eV. In addition, two shake-up satellite peaks (indicated by "Sat.") are also observed at 941.7 and 962.1 eV (Fig. 2c), hence confirming the $Cu^{2+}$ characteristic.[39, 40] In the Mn 2p spectrum (Fig. 2b), two types of manganese species are detected and attributed to species containing $Mn^{2+}$ and $Mn^{3+}$ ions. Specifically, the fitting peaks at 641.5 and 653.4 eV are assigned to $Mn^{2+}$, and the peaks at 643.5 and 654.5 eV are ascribed to the existence of $Mn^{3+}$.[41] Similarly, the Co 2p spectrum (Fig. 2c) consists of Co 2p3/2 and Co 2p1/2 at 780.0 and 795.1 eV, respectively, together with a spin-energy separation of around 15 eV, thereby indicating the presence of the mixed $Co^{2+}$ and $Co^{3+}$.[40, 42] The fitting peaks at around 779.6 and 794.8 eV are ascribed to $Co^{2+}$, and the peaks at 782.4 and 796.1 eV represent the $Co^{3+}$.[39] The two shake-up satellite peaks located approximately 788.2 and 803.3 eV reveal that cobalt has a spinel structure.[32, 39] The high-resolution spectrum of the O 1s region (Fig. 2d) shows three oxygen contributions, which are marked with O1, O2, and O3. Notably, the O1 component at 529.4 eV is consistent with typical metal–oxygen bonds.[3] The well-resolved O2 component at approximately 531.1 eV corresponds to a larger number of defect sites with low oxygen coordination.[31, 43] The O3 component at 532.6 eV is assigned to the multiplicity of physi- and chemisorbed water at or near the surface.[31, 43] These results clearly show that the chemical compositions of the prepared $CuCo_2O_4/MnCo_2O_4$ heterostructures contain $Co^{2+}$, $Co^{3+}$, $Mn^{2+}$, $Mn^{3+}$, and $Cu^{2+}$.

Fig. 3 presents the morphology of the as-obtained spinel $CuCo_2O_4$ and $CuCo_2O_4/MnCo_2O_4$ heterostructures on the graphite paper. The sphere-like $CuCo_2O_4$ is composed of uniform

nanosheets with the length and diameter of 1.2 μm and 45 nm, respectively (Fig. 3a–c). These nanosheets are highly interconnected and radially protruding outward in all directions on the graphite paper, thus forming an open porous networks, which favors electrolyte ion penetration and electron transport. By contrast, the bilayer $CuCo_2O_4/MnCo_2O_4$ heterostructures show an open network structure of $MnCo_2O_4$ nanosheets oriented perpendicularly to the surface of $CuCo_2O_4$ nanosheets. Fig. 3d–f show $CuCo_2O_4/MnCo_2O_4$ heterostructures where $MnCo_2O_4$ nanosheets (length, 3.4 μm; thickness, 238 nm) were grown on top of $CuCo_2O_4$ material. Such structural and morphological characteristics of $CuCo_2O_4/MnCo_2O_4$ is expected to provide more electroactive sites for redox reaction and facilitate channels between electron and ion transport to enhance the capacitive mechanism. Furthermore, SEM images show that $CuCo_2O_4/MnCo_2O_4$ heterostructures provide a much higher density compared with $CuCo_2O_4$ structure. This result proves that the two-step hydrothermal approach is effective in increasing the loading mass of active materials and preserves the distinct structural morphology of electroactive materials. The isotherms and porosity of the obtained $CuCo_2O_4$ and $CuCo_2O_4/MnCo_2O_4$ heterostructures were investigated through nitrogen adsorption–desorption experiments at 77 K. The specific surface areas were calculated using the BET equation. Fig. S7 (a) shows the nitrogen adsorption–desorption isotherms of $CuCo_2O_4$ and $CuCo_2O_4/MnCo_2O_4$ heterostructures. The isotherms can be classified as type IV curve with a hysteresis loop,[44] indicating the samples are mesoporous materials. The isotherms show that the vertically stacked bilayer $CuCo_2O_4/MnCo_2O_4$ heterostructures possess a higher specific surface area of about 80.8 $m^2\ g^{-1}$ than that of the microsphere-like $CuCo_2O_4$ nanosheets (~ 52.0 $m^2\ g^{-1}$). Fig. S7 (b) shows the pore distribution curves of samples, indicating that the bilayer $CuCo_2O_4/MnCo_2O_4$ heterostructures possess significant amount of mesoporous pores compared with the $CuCo_2O_4$ sample. Such high BET

specific surface area and significant amount of mesoporous pores could largely enrich the electroactive sites and shorten the diffusion paths for charge transports, which facilitate to enhance the electrochemical capacity.

TEM is further performed to investigate the structure of $CuCo_2O_4$ and $MnCo_2O_4$ nanosheets. $CuCo_2O_4$ nanosheets possess a highly porous texture, continuous vermiculate holes, and an ultrathin feature (Fig. 4). The magnified images (Fig. 4b) clearly show white spots (4–10 nm), thereby indicating that the pores are uniformly distributed throughout the nanosheet surface. The formation of the pores could be related to the release of gas or water molecules during the thermal decomposition of the $CuCo_2O_4$ precursor. Flower-like $CuCo_2O_4$ nanosheets exhibit transparent features, which indicate their ultrathin nature; these features are consistent with those observed under SEM. Ultrathin nanosheets with large electroactive surface areas and open-network features can ensure an efficient and rapid diffusion of electrolyte ions to the active material surface; consequently, more electroactive sites exist for Faradaic reactions, hence leading to high specific capacitance.[45] Fig. 4b shows some visible lattice fringes with an equal interplanar distance of 0.208 nm, which corresponds to the (400) planes of cubic $CuCo_2O_4$ and further confirms the formation of crystalline $CuCo_2O_4$ nanosheets. In addition, the corresponding selected area electron diffraction (SAED) pattern in Fig. 4c indicates the polycrystalline structure of the nanosheets, and the diffraction rings can be readily indexed to the (311), (400), and (440) planes of the $CuCo_2O_4$ phase. These results are consistent with the XRD patterns. Moreover, the TEM images of the upper layer $MnCo_2O_4$ nanosheets are shown (Fig. 4d). These nanosheets consist of a large quantity of pores with diameters within the range of 8–16 nm, which indicates highly porous nature. Fig. 4e shows some visible lattice fringes with equal interplanar distances

of 0.208 and 0.244 nm that correspond to the (400) and (311) planes of cubic $MnCo_2O_4$, respectively. In addition, (111) plane with an equal interplanar distance of 0.473 nm makes an angle of 58.5° with (311), further confirming the formation of crystalline $MnCo_2O_4$ nanosheets. The SAED pattern of $MnCo_2O_4$ (Fig. 4f) also shows the well-defined diffraction rings of (111), (220), (311), (222), and (400) planes, thus confirming the polycrystalline nature of the $MnCo_2O_4$ nanosheets.

To evaluate the electrochemical performance of the proposed vertically stacked bilayer $CuCo_2O_4/MnCo_2O_4$ heterostructures as superior electrodes in electrochemical capacitor, the CV curves of $CuCo_2O_4$ and $CuCo_2O_4/MnCo_2O_4$ heterostructure electrodes are obtained at scan rates of 2, 5, 10, and 20 mV $s^{-1}$, with potential windows that range from −0.2 V to 0.6 V in a 2 M KOH solution (Figs. 5a,b). The $CuCo_2O_4$ electrode exhibits a pair of redox peaks at 0.24 and 0.36 V, which can be attributed to the redox reactions related to $Co^{2+}/Co^{3+}/Co^{4+}$ and $Cu^{2+}/Cu^{+}$ associated with $OH^{-}$ anions.[46, 47] The peak current evidently increases with increasing scan rate, thereby suggesting a rapid diffusion-controlled electrolyte ion transport kinetic at the interface. These well-defined redox peaks of $CuCo_2O_4/MnCo_2O_4$ can be observed at low scan rates, which mainly originate from the Faradaic redox reactions that are related to M–O/M–O–OH (M represents Mn and Co ions)[41, 48] and Cu–O/Cu–OH associated with anion $OH^{-}$;[46, 47] these results indicate the typical Faradaic characteristics of the as-prepared electrode materials. A coupled pair of redox peaks at 0.24/0.37 V (I/II) may also be related to the Faradaic behavior of $CuCo_2O_4$.[46, 47] Additionally, a second pair of redox peaks at 0.30/0.44 V (III/IV) is observed, which reveals the plausible reversible transition between $MnCo_2O_4$ and MnOOH/CoOOH and transition between CoOOH and $CoO_2$.[41, 48] Results clearly show that the proposed

$CuCo_2O_4/MnCo_2O_4$ bilayer heterostructures offer a richer electrochemical performance compared with a single spinel structure. With the 10-fold increase in the sweep rate from 2 mV $s^{-1}$ to 20 mV $s^{-1}$, the position of the cathodic peaks shifts slightly from 0.25 V to 0.18 V. This shift corresponds to the increase in internal resistance to ion and electron transfer at higher scan rates, and such internal resistance increase causes a slight decrease in the electrochemical performance.[49] Fig. 5c shows the CV curves of the bare graphite paper, $CuCo_2O_4$, and $CuCo_2O_4/MnCo_2O_4$ electrodes at the scan rate of 20 mV $s^{-1}$. Variations of redox peak positions can be observed from the two samples, which may be ascribed to the difference in electrode polarization behavior during the tests. Specifically, the polarization behavior is closely related to the chemical composition and physical morphology of the electrode material.[50] A significantly larger integrated area of the CV curve is observed in $CuCo_2O_4/MnCo_2O_4$ electrode, thereby indicating that the vertically stacked $CuCo_2O_4/MnCo_2O_4$ heterostructures have higher electrochemical reaction activity. The superior electrochemical properties of $CuCo_2O_4/MnCo_2O_4$ heterostructures are attributed to the distinct bilayer heterostructures providing an additional contact interface of electrode/electrolyte and richer Faradaic reaction through the $MnCo_2O_4$ material. The CV curve of bare graphite paper provides a negligible contribution to the entire electrode capacitance (about 8.43% and 4.74% for $CuCo_2O_4$ and $CuCo_2O_4/MnCo_2O_4$ heterostructures, respectively). The cathodic peak current densities of $CuCo_2O_4$ and $CuCo_2O_4/MnCo_2O_4$ electrodes (Fig. 5d) are plotted as functions of the square roots of the scan rates ($v^{1/2}$). The cathode peak current increases linearly with the square root of scan rates, which satisfies Cottrell equation and indicates a diffusion-controlled non-surface process.[51, 52] Specifically, the apparent diffusion coefficient ($D$) of $OH^-$ ion is calculated in prepared materials by employing Randles–Sevcik equation 10.[52]

$$I_p = 2.69 \times 10^5 \times n^{\frac{3}{2}} \times A \times \sqrt{D} \times C \times \sqrt{v} \quad (10)$$

$$D(\mathrm{CuCo_2O_4/MnCo_2O_4})/D(\mathrm{CuCo_2O_4}) = [(I_p/\sqrt{v})(\mathrm{CuCo_2O_4/MnCo_2O_4})/(I_p/\sqrt{v})(\mathrm{CuCo_2O_4})]^2 = (11.99/6.78)^2 = 3.13 \quad (11)$$

where $I_p$ is the peak current, $n$ is the number of electrons involved in the reaction, $A$ is the surface area of the electrode, $D$ is the diffusion coefficient of the electrode material, $C$ is the proton concentration, and $v$ is the scanning rate. The diffusion coefficient of the $CuCo_2O_4/MnCo_2O_4$ heterostructure electrode ($D_{CuCo2O4/MnCo2O4}$) is around 3.13 times larger than that of the $CuCo_2O_4$ electrode ($D_{CuCo2O4}$), hence indicating its higher ion mobility.

The galvanostatic charge/discharge curves of bilayer $CuCo_2O_4/MnCo_2O_4$ heterostructure electrode and $CuCo_2O_4$ nanosheet electrode are carried out within the voltage range of 0–0.6 V at various current densities (Figs. 6a, b). The discharge capacitances of the $CuCo_2O_4/MnCo_2O_4$ electrode are much higher than those of the $CuCo_2O_4$ electrodes, which is in accordance with the aforementioned CV results. Rate capability is a critical parameter of electrochemical capacitors for assessing their application potential. Fig. 6b shows the galvanostatic charge/discharge plot of $CuCo_2O_4/MnCo_2O_4$ electrode at different current densities (0.5, 1, 2, 3, 5, 10, and 15 A $g^{-1}$). Consistent with the CV results, the cathodic peak at about 0.45 V is well manifested as voltage plateaus from the galvanostatic discharge curves of $CuCo_2O_4/MnCo_2O_4$. With higher current densities, this plateau shifts to a higher voltage because of stronger polarization effect.[53] The discharge capacitance performance is calculated from the galvanostatic charge/discharge curves, as shown in Fig. 6c. The specific capacitances decrease gradually with increasing current densities, which proves that the kinetics of the redox reaction is governed mainly by the migration and diffusion of ions in the electrolyte.[54] On the contrary, the diffusion and migration

of electrolytic ions are suppressed at high current density, thus leading to the inefficacy of the inner active surface area for charge storage in this battery-type materials.[55] To easily create a contrast with previous reported works, we present the data as specific capacitance. Impressively, the $CuCo_2O_4/MnCo_2O_4$ electrode exhibits the discharge capacitance of 1434 F $g^{-1}$ at 0.5 A $g^{-1}$ and still maintains 810 F $g^{-1}$ at 15 A $g^{-1}$, whereas the $CuCo_2O_4$ electrode shows the discharge capacitance of 975 and 488 F $g^{-1}$ at 0.5 and 15 A $g^{-1}$, respectively. In addition, $CuCo_2O_4/MnCo_2O_4$ heterostructure electrode exhibits better rate capability, with 56.6% capacitance retention when the current density increases by a factor of 30 (from 0.5 A $g^{-1}$ to 15 A $g^{-1}$) compared with the 50.1% capacitance retention of $CuCo_2O_4$ electrode. Long-term cycling stability is an important criterion for practical supercapacitor applications. Fig. 6d presents the cycling performance of the $CuCo_2O_4$ and $CuCo_2O_4/MnCo_2O_4$ bilayer heterostructure electrodes. The $CuCo_2O_4$ electrode exhibits a specific capacitance of 449 A $g^{-1}$ (~76.6% capacitance retention) after 5000 cycles at a current density of 10 A $g^{-1}$, whereas the $CuCo_2O_4/MnCo_2O_4$ electrode exhibits an impressive higher capacitance of 848 F $g^{-1}$ (~81.4% capacitance retention) after 5000 cycles at a current density of 10 A $g^{-1}$. After 5000 cycles, the Columbic efficiency of $CuCo_2O_4/MnCo_2O_4$ electrode remains 98.4% (Fig. S6). The proposed $CuCo_2O_4/MnCo_2O_4$ heterostructure electrode plays an important role in achieving high specific capacitance. In particular, (1) considerable spaces between the interconnected open-network nanosheet arrays shorten the diffusion distance from the external electrolyte to the interior surface and improve the utilization rate of electrode materials;[49] (2) direct contact of $CuCo_2O_4/MnCo_2O_4$ heterostructures on the highly conductive graphite paper not only avoids the use of polymer binder/conductive additives and reduces the "dead volume" in the electrode substantially, but also favors the effective electron transfer;[56] (3) the distinct thinness of the nanosheet can ensure high-rate

performance;[57] and (4) bilayer heterostructures preserve the distinctive structure integrity of $CuCo_2O_4$ and $MnCo_2O_4$ phases, which leads to superior electrochemical performances.[57] To the best of our knowledge, the discharge capacitance performance of the $CuCo_2O_4/MnCo_2O_4$ bilayer heterostructure electrode reported in this study is much higher than that of conventional carbonaceous materials, as well as higher than most of previously reported cauliflower-like $CuCo_2O_4$ nanoparticle (338F $g^{-1}$ at 1 A $g^{-1}$),[46] core–shell $CuCo_2O_4/MnO_2$ heterostructured nanowire (714 mF $cm^{-2}$ at 1 mA $cm^{-2}$),[58] $MnCo_2O_4$ nanoparticles (405 F $g^{-1}$ at 5 mA $cm^{-2}$),[59] and Mn–Ni–Co ternary oxide nanowire (638 F $g^{-1}$ at 1 A $g^{-1}$).[59] Such high discharge capacitance of the $CuCo_2O_4/MnCo_2O_4$ bilayer heterostructure electrodes could be derived from the distinct advantages. First, the vertical stacking approach can increase the mass loading of active materials, thereby resulting in the more active sites of multiple spinel phases for electrochemical reactions, which leads to faster kinetics in electron and ion transportation. Second, the stepwise growth of nanostructures prevents the aggregation of the phases and preserves the open network of individual nanostructure. Third, large spaces among the interface of vertical stacking nanostructures allow easy access of electrolyte to the multiple spinel phases, hence facilitating ion diffusion at the electrode/electrolyte interface. Fourth, stepwise growth of nanostructures ensures good mechanical adhesions between multiple spinel phases, thus ensuing good electrical conductivity of the heterostructures.

EIS is conducted to evaluate the ion transport kinetics further at the electrode/electrolyte interface. Fig. 6e presents the impedance Nyquist plots of the samples. The bottom-left inset in Fig. 6e shows the fitted equivalent circuit for the measured impedance data. The high-frequency intercept of the semicircle on the real axis shows the series resistance ($R_s$), and the diameter of

the semicircle corresponds to the charge-transfer resistance ($R_{ct}$) of the Faradaic process. Fig. 6e clearly shows that the $CuCo_2O_4/MnCo_2O_4$ electrode has a lower $R_s$ (1.56 Ω) than the $CuCo_2O_4$ electrode (10.42 Ω). Moreover, the impedance spectrum of the $CuCo_2O_4/MnCo_2O_4$ electrode reveals a smaller semicircle, which indicates that the $R_{ct}$ of $CuCo_2O_4/MnCo_2O_4$ electrode (1.29 Ω) is lower than that of the $CuCo_2O_4$ electrode (3.62 Ω), thereby suggesting that the $CuCo_2O_4/MnCo_2O_4$ electrode has a higher electrochemical activity. In the low-frequency region, the $CuCo_2O_4/MnCo_2O_4$ electrode shows a more ideal straight line, which indicates a more efficient electrolyte and proton diffusion.[60] More importantly, the slope of the linear part of the $CuCo_2O_4/MnCo_2O_4$ electrode shows no significant change after cycling, which implies the good ionic diffusion and access to the electrolyte after cycling. These results may be caused by the ultrathin feature of the nanosheets and interconnected open network $CuCo_2O_4/MnCo_2O_4$ architecture, which leads to an enhanced ionic diffusion and charge transport. After 5000 cycles, the $R_{ct}$ of the $CuCo_2O_4/MnCo_2O_4$ electrode slightly increases from 1.56 Ω to 3.14 Ω, hence implying a small interfacial charge transfer resistance and excellent cycling stability. The enhanced electrochemical properties of the $CuCo_2O_4/MnCo_2O_4$ electrode are attributed to the robustness of the interconnected open network. This phenomenon prevents structural degradation and facilitates rapid ion and electron transfer within the electrode and at the electrode–electrolyte interface. Results clearly demonstrate that the rational design of bilayer $CuCo_2O_4/MnCo_2O_4$ heterostructure electrode displays a favorable charge-transfer kinetics and rapid electron transport, and thus exhibits the dramatically enhanced electrochemistry performance.

Fig. 7a shows the CV curves of the assembled electrochemical capacitor at a scan rate of 50 mV $s^{-1}$ at different potential windows. The assembled electrochemical capacitor exhibits quasi-

rectangular-shaped CV curves coupled with a pair of redox peaks resulting from Faradaic reactions that occur on $CuCo_2O_4/MnCo_2O_4$ electrode. As the potential window is extended to 1.6 V, an undesirable oxygen revolution reaction-induced peak is clearly observed. This finding suggests that the electrochemical capacitor can deliver a maximum working voltage of 1.6 V. Therefore, 1.6V is used as the default voltage value for further investigation. Fig. 7b demonstrates the CV curves of the device at different scan rates. CV profiles still retain a relatively rectangular shape without serious distortion when the scan rates are increased, thereby suggesting a quick I–V response and good reversible energy storage ability. The charge/discharge curves of the electrochemical capacitor at various current densities and corresponding specific capacitances are shown in Figs. 7c and 7d, respectively. The device delivers a specific capacitance of 118.4 F $g^{-1}$ at a current density of 0.5 A $g^{-1}$, which is higher than the other specific capacitance values reported for electrochemical capacitor. As the discharge current densities increase to 1, 1.5, 2, 2.5, 5, 7.5, and 10 A $g^{-1}$, high specific capacitances of 100.6, 90.9, 82.4, 76.6, 56.3, 46.4, and 37.5 F $g^{-1}$ are achieved, respectively, thus implying a good rate capability.

To further evaluate the present electrochemical capacitor for practical application, Fig. 8a illustrates the button cell using graphene/NF and $CuCo_2O_4/MnCo_2O_4$ heterostructures as negative and positive electrodes, respectively, with a piece of cellulose paper as the separator. The high capacitance value of the assembled device is closely related to the high specific capacitance of positive and negative electrodes. Based on the charge/discharge curves, the energy and power densities for the $CuCo_2O_4/MnCo_2O_4$//graphene/NF electrochemical capacitor at various current densities are shown in the Ragone plots (Fig. 8b). Remarkably, the present device delivers a

maximum energy density of about 42.1 Wh $kg^{-1}$ at a power density of 400 W $kg^{-1}$. This energy density is significantly larger than those of symmetric supercapacitors reported to date, such as $CoMn_2O_4$/graphene//$CoMn_2O_4$/graphene (18 Wh $kg^{-1}$)[61] and $Co(OH)_2$//$Co(OH)_2$ supercapacitors (3.96 Wh $kg^{-1}$),[62] and also larger than those of asymmetric electrochemical capacitors, such as $Co_3O_4$//AC (34 Wh $kg^{-1}$ at 225 W $kg^{-1}$),[59] rGO-NiCo oxide//AC (23.32 Wh $kg^{-1}$ at 324.9 W $kg^{-1}$),[63] $CoMn_2O_4$//graphene (7.4 Wh $kg^{-1}$ at 1.90 kW $kg^{-1}$),[61] $NiCo_2O_4$/$MnO_2$//AC (35 Wh $kg^{-1}$ at 163 W $kg^{-1}$),[16] $Ni_xCo_{3-x}$ oxide//AC (37.4 Wh $kg^{-1}$ at 163 W $kg^{-1}$),[64] $Co(OH)_2$/$Co_3O_4$//AC (22.4 Wh $kg^{-1}$ at 290 W $kg^{-1}$),[65] and $NiCo_2S_4$//AC (25.5 Wh $kg^{-1}$ at 334 W $kg^{-1}$).[66] Even at a high power density of 7.9 kW $kg^{-1}$, the device can still reach an energy density of 13.3 Wh $kg^{-1}$, which indicates good power capability. Fig. 8c shows the capacitance retention of the present device as a function of cycle number at a current density of 5 A $g^{-1}$ for 10000 charge/discharge cycles. Results clearly show that 88.4% of its initial capacitance is retained after 10000 cycles, hence indicating a good cycling stability for electrochemical capacitor.

## Conclusions

In this study, we developed a two-step hydrothermal growth process to prepare vertically stacked bilayer $CuCo_2O_4$/$MnCo_2O_4$ heterostructures on functionalized graphite paper substrate and demonstrate its application as superior electrodes for high-performance electrochemical capacitors. In these distinct heterostructures, the microsphere-like $CuCo_2O_4$ that consists of nanosheets not only acts as an excellent battery type material but also serves as a hierarchical scaffold capable of rapid electron conduction and ion diffusion for the growth of additional electroactive materials $MnCo_2O_4$. $CuCo_2O_4$/$MnCo_2O_4$ electrode exhibits enhanced specific capacitance, high rate capability, and excellent cycling stability. Furthermore, the assembled

$CuCo_2O_4/MnCo_2O_4$//graphene/NF hybrid device delivers a high energy density of 42.1 Wh $kg^{-1}$ at a power density of 400 W $kg^{-1}$ and still maintain an energy density of 13.3Wh $kg^{-1}$ at an outstanding power density of 7.9 kW $kg^{-1}$. The device also shows an excellent cycling stability with 88.4% of initial capacitance retained after 10000 cycles. The rational vertical stacking architecture design could open a new design approach for high-performance electrode materials for next-generation energy storage applications.

**Acknowledgements**

This work was supported by the Basic Science Research Program through the National Research Foundation of Korea (NRF) funded by the Ministry of Education, Science and Technology (2014R1A1A2055740), Global Frontier Program through the Global Frontier Hybrid Interface Materials (GFHIM) program of the National Research Foundation of Korea (NRF) funded by the Ministry of Science, ICT & Future Planning (2013M3A6B1078874), and the Start-up Research Grant (SRG2015-00057-FST) from Research & Development Office at University of Macau.

## References


1. C. Yuan, H. B. Wu, Y. Xie and X. W. D. Lou, *Angew. Chem. Int. Ed.*, 2014, **53**, 1488.
2. J. Yang, C. Yu, X. Fan and J. Qiu, *Adv. Energy Mater.*, 2014, **4**, 1400761.
3. C. Yuan, J. Li, L. Hou, X. Zhang, L. Shen and X. W. D. Lou, *Adv. Energy Mater.*, 2012, **22**, 4592.
4. L. Yu, G. Zhang, C. Yuan and X. W. D. Lou, *Chem. Commun.*, 2013, **49**, 137.
5. J. Yan, Z. Fan, W. Sun, G. Ning, T. Wei, Q. Zhang, R. Zhang, L. Zhi and F. Wei, *Adv. Funct. Mater.*, 2012, **22**, 2632.
6. M. K. Zate, S. M. F. Shaikh, V. V. Jadhav, K. K. Tehare, S. S. Kolekar, R. S. Mane, M. Naushad, B. N. Pawar and K. N. Hui, *J. Anal. Appl. Pyrolysis*, 2015, **116**, 177.
7. S. Liu, K. O. Hui and K. Hui, *ACS Appl. Mater. Interfaces*, 2016, **8**, 3258.
8. B. Liu, B. Liu, Q. Wang, X. Wang, Q. Xiang, D. Chen and G. Shen, *ACS Appl. Mater. Interfaces*, 2013, **5**, 10011.
9. S. Dou, *Ionics*, 2015, **21**, 3001.
10. T. R. Paudel, A. Zakutayev, S. Lany, M. d'Avezac and A. Zunger, *Adv. Funct. Mater.*, 2011, **21**, 4493.
11. E. F. Schubert, *Doping in III-V semiconductors*, Cambridge University Press, 2005.
12. H. Hua, S. Liu, Z. Chen, R. Bao, Y. Shi, L. Hou, G. Pang, K. N. Hui, X. Zhang and C. Yuan, *Sci. Rep.*, 2016, **6**, 20973.
13. S. Liu, K. S. Hui and K. N. Hui, *ChemNanoMat*, 2015, **1**, 593.
14. C. Yuan, H. Cao, S. Zhu, H. Hua and L. Hou, *J. Mater. Chem. A*, 2015, **3**, 20389.
15. L. Hou, L. Lian, L. Zhang, G. Pang, C. Yuan and X. Zhang, *Adv. Funct. Mater.*, 2015, **25**, 238.
16. K. Xu, W. Li, Q. Liu, B. Li, X. Liu, L. An, Z. Chen, R. Zou and J. Hu, *J. Mater. Chem. A*, 2014, **2**, 4795.
17. L. Zhang, K. N. Hui, K. San Hui and H. Lee, *Electrochim. Acta*, 2015, **186**, 522.
18. C. Yuan, J. Li, L. Hou, J. Lin, X. Zhang and S. Xiong, *J. Mater. Chem. A*, 2013, **1**, 11145.
19. F. Luan, G. Wang, Y. Ling, X. Lu, H. Wang, Y. Tong, X. X. Liu and Y. Li, *Nanoscale*, 2013, **5**, 7984.
20. R. R. Salunkhe, S. H. Hsu, K. C. Wu and Y. Yamauchi, *ChemSusChem*, 2014, **7**, 1551-1556.
21. R. R. Salunkhe, J. Lin, V. Malgras, S. X. Dou, J. H. Kim and Y. Yamauchi, *Nano Energy*, 2015, **11**, 211.
22. R. R. Salunkhe, Y. Kamachi, N. L. Torad, S. M. Hwang, Z. Sun, S. X. Dou, J. H. Kim and Y. Yamauchi, *J. Mater. Chem. A*, 2014, **2**, 19848.
23. L. J. Zhang, J. Wang, J. J. Zhu, X. G. Zhang, K. S. Hui and K. N. Hui, *J. Mater. Chem. A*, 2013, **1**, 9046.
24. K. Cao, L. Jiao, H. Liu, Y. Liu, Y. Wang, Z. Guo and H. Yuan, *Adv. Energy Mater.*, 2015, **5**, 140142.
25. S. Liu, K. S. Hui, K. N. Hui, V. V. Jadhav, Q. X. Xia, J. M. Yun, Y. R. Cho, R. S. Mane and K. H. Kim, *Electrochim. Acta*, 2016, **188**, 898.
26. H. Hua, S. Liu, Z. Chen, R. Bao, Y. Shi, L. Hou, G. Pang, K. N. Hui, X. Zhang and C. Yuan, *Sci. Rep.*, 2016, **6**, 20973.
27. K. Kakaei and K. Hasanpour, *J. Mater. Chem. A*, 2014, **2**, 15428.
28. L. C. Sim, K. H. Leong, S. Ibrahim and P. Saravanan, *J. Mater. Chem. A*, 2014, **2**, 5315.

29. M. Naebe, J. Wang, A. Amini, H. Khayyam, N. Hameed, L. H. Li, Y. Chen and B. Fox, *Sci. Rep.*, 2014, **4**, 4375.
30. B. Dehghanzad, M. K. R. Aghjeh, O. Rafeie, A. Tavakoli and A. J. Oskooie, *RSC Adv.*, 2016, **6**, 3578.
31. Y. Lei, J. Li, Y. Wang, L. Gu, Y. Chang, H. Yuan and D. Xiao, *ACS Appl. Mater. Interfaces*, 2014, **6**, 1773.
32. Q. Liao, N. Li, S. Jin, G. Yang and C. Wang, *ACS Nano*, 2015, **9**, 5310.
33. M. A. Prathap, C. Wei, S. Sun and Z. J. Xu, *Nano Res.*, 2015, **8**, 2636.
34. J. Lee, K. N. Hui, K. S. Hui, Y. R. Cho and H. H. Chun, *Appl. Surf. Sci.*, 2014, **293**, 55.
35. X.-h. Xia, J.-p. Tu, Y.-q. Zhang, Y.-j. Mai, X.-l. Wang, C.-d. Gu and X.-b. Zhao, *RSC Adv.*, 2012, **2**, 1835.
36. G. Zhu, C. Xi, M. Shen, C. Bao and J. Zhu, *ACS Appl. Mater. Interfaces*, 2014, **6**, 17208.
37. R. Ding, L. Qi and H. Wang, *Electrochim. Acta*, 2013, **114**, 726.
38. X.-h. Xia, J.-p. Tu, Y.-j. Mai, X.-l. Wang, C.-d. Gu and X.-b. Zhao, *J. Mater. Chem.*, 2011, **21**, 9319.
39. S. Vijayakumar, S.-H. Lee and K.-S. Ryu, *Electrochim. Acta*, 2015, **182**, 979.
40. J. Zhu and Q. Gao, *Microporous Mesoporous Mater.*, 2009, **124**, 144.
41. L. Li, F. He, S. Gai, S. Zhang, P. Gao, M. Zhang, Y. Chen and P. Yang, *CrystEngComm*, 2014, **16**, 9873.
42. R. Ning, J. Tian, A. M. Asiri, A. H. Qusti, A. O. Al-Youbi and X. Sun, *Langmuir*, 2013, **29**, 13146.
43. R. Zou, K. Xu, T. Wang, G. He, Q. Liu, X. Liu, Z. Zhang and J. Hu, *J. Mater. Chem. A*, 2013, **1**, 8560.
44. Q. X. Xia, K. S. Hui, K. N. Hui, S. D. Kim, J. H. Lim, S. Y. Choi, L. J. Zhang, R. S. Mane, J. M. Yun and K. H. Kim, *J. Mater. Chem. A*, 2015, **3**, 22102.
45. D. P. Dubal, P. Gomez-Romero, B. R. Sankapal and R. Holze, *Nano Energy*, 2015, **11**, 377.
46. A. Pendashteh, M. S. Rahmanifar, R. B. Kaner and M. F. Mousavi, *Chem. Commun.*, 2014, **50**, 1972.
47. A. Pendashteh, S. E. Moosavifard, M. S. Rahmanifar, Y. Wang, M. F. El-Kady, R. B. Kaner and M. F. Mousavi, *Chem. Mater.*, 2015, **27**, 3919.
48. A. K. Mondal, D. Su, S. Chen, A. Ung, H. S. Kim and G. Wang, *Chem. Eur. J.*, 2015, **21**, 1526.
49. D. P. Cai, D. D. Wang, B. Liu, L. L. Wang, Y. Liu, H. Li, Y. R. Wang, Q. H. Li and T. H. Wang, *ACS Appl. Mater. Interfaces*, 2014, **6**, 5050.
50. Y. Chen, B. Qu, L. Hu, Z. Xu, Q. Li and T. Wang, *Nanoscale*, 2013, **5**, 9812.
51. L. Ren, K. S. Hui and K. N. Hui, *J. Mater. Chem. A*, 2013, **1**, 5689.
52. S. Liu, K. S. Hui and K. N. Hui, *ACS Appl. Mater. Interfaces*, 2016, **8**, 3258.
53. Q. Chu, W. Wang, X. Wang, B. Yang, X. Liu and J. Chen, *J. Power Sources*, 2015, **276**, 19.
54. K. Chen, S. Song, K. Li and D. Xue, *CrystEngComm*, 2013, **15**, 10367.
55. T. Brousse, D. Bélanger and J. W. Long, *J. Electrochem. Soc.*, 2015, **162**, A5185.
56. L. Zhang, K. N. Hui, K. S. Hui and H. Lee, *Electrochim. Acta*, 2015, **186**, 522.
57. S. Liang, Y. Hu, Z. Nie, H. Huang, T. Chen, A. Pan and G. Cao, *Nano Energy*, 2015, **13**, 58.

58. C. Nethravathi, C. R. Rajamathi, M. Rajamathi, X. Wang, U. K. Gautam, D. Golberg and Y. Bando, *ACS Nano*, 2014, **8**, 2755.
59. L.-B. Kong, C. Lu, M.-C. Liu, Y.-C. Luo, L. Kang, X. Li and F. C. Walsh, *Electrochim. Acta*, 2014, **115**, 22.
60. S. X. Wu, K. S. Hui and K. N. Hui, *J. Phys. Chem. C*, 2015, **119**, 23358.
61. P. Ahuja, V. Sahu, S. K. Ujjain, R. K. Sharma and G. Singh, *Electrochim. Acta*, 2014, **146**, 429.
62. A. Jagadale, V. Kumbhar, D. Dhawale and C. Lokhande, *Electrochim. Acta*, 2013, **98**, 32-38.
63. X. Wang, W. S. Liu, X. Lu and P. S. Lee, *J. Mater. Chem.*, 2012, **22**, 23114-23119.
64. X. Wang, C. Yan, A. Sumboja and P. S. Lee, *Nano Energy*, 2014, **3**, 119.
65. M. Jing, Y. Yang, Y. Zhu, H. Hou, Z. Wu and X. Ji, *Electrochim. Acta*, 2014, **141**, 234.
66. Z. Wu, X. Pu, X. Ji, Y. Zhu, M. Jing, Q. Chen and F. Jiao, *Electrochim. Acta*, 2015, **174**, 238.

Fig. 1

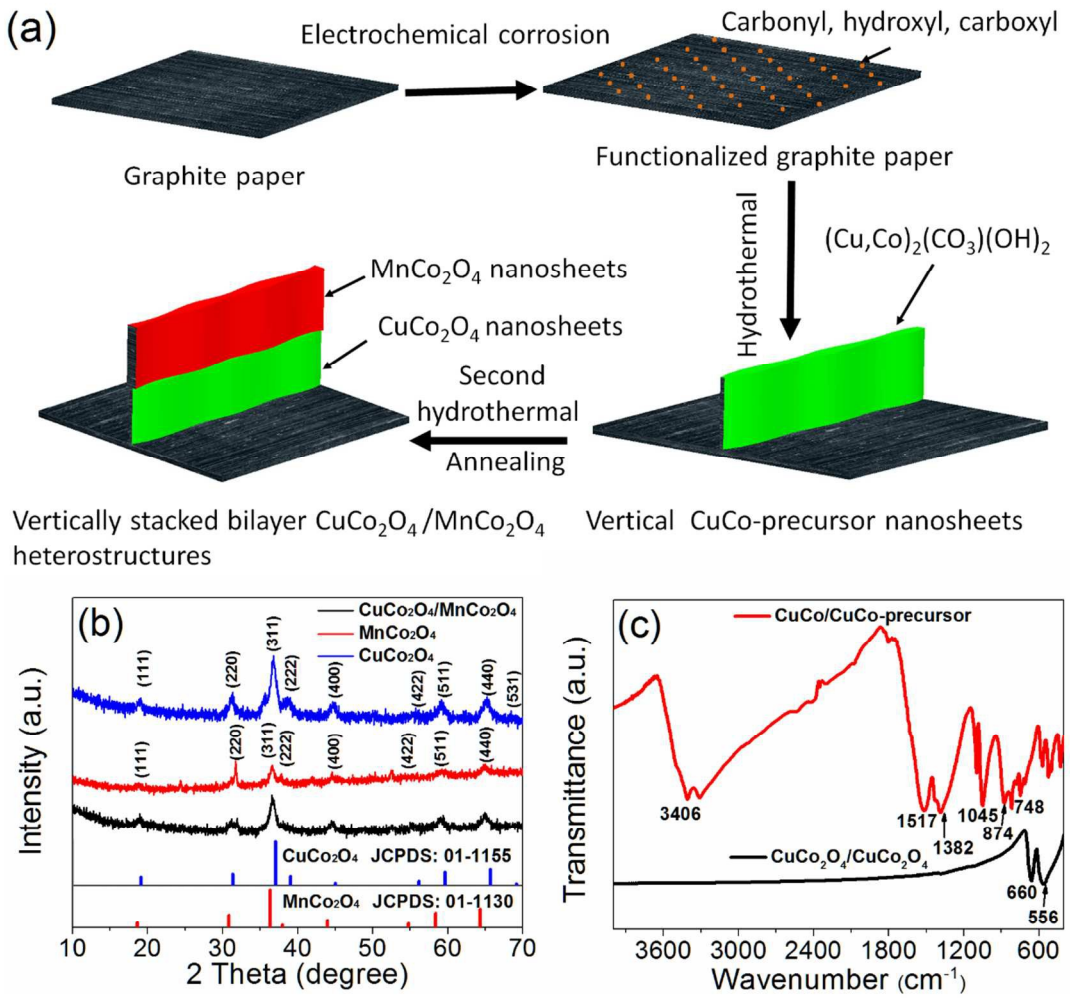


Fig. 1 (a) Schematic for the synthesis of vertically stacked bilayer $CuCo_2O_4/MnCo_2O_4$ heterostructures on functionalized graphite paper. (b) XRD patterns of the as-prepared products. (c) Fourier transform infrared spectra of $CuCo_2O_4/MnCo_2O_4$ before and after annealing.

Fig. 2

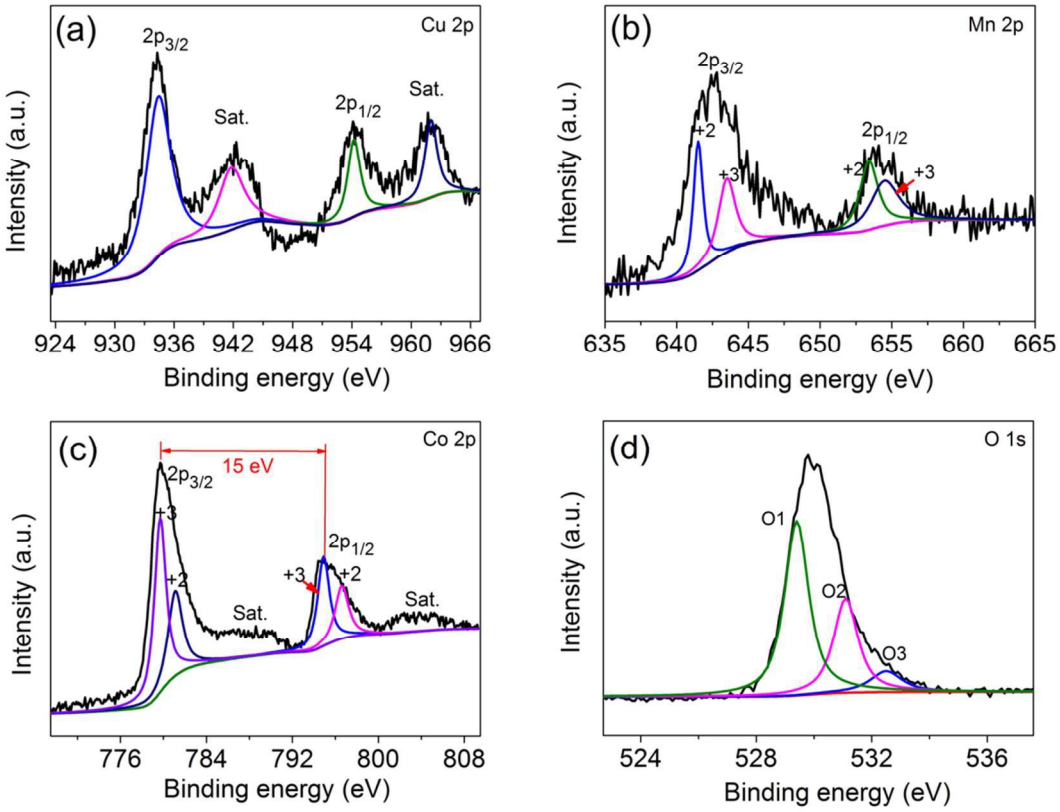


Fig. 2 X-ray photoelectron spectroscopy spectra of bilayer $CuCo_2O_4/MnCo_2O_4$ heterostructures: (a) Cu 2p, (b) Mn 2p, (c) Co 2p, and (d) O1s.

Fig. 3

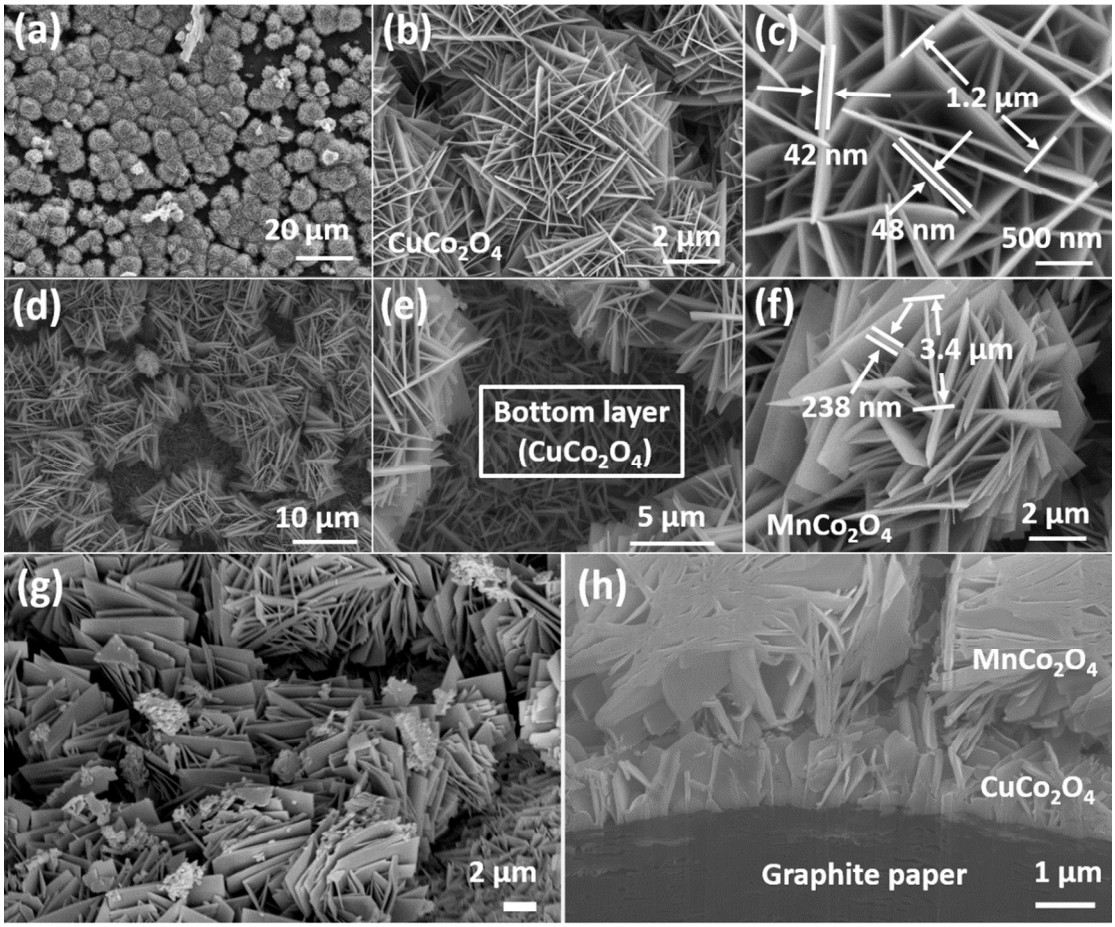


Fig. 3 (a–c) FESEM images of microsphere-like $CuCo_2O_4$ nanosheets, (d–f) vertically stacked bilayer $CuCo_2O_4/MnCo_2O_4$ heterostructures, (g) FESEM and (h) FIB images of the bilayer heterostructures tilted at 54°.

Fig. 4

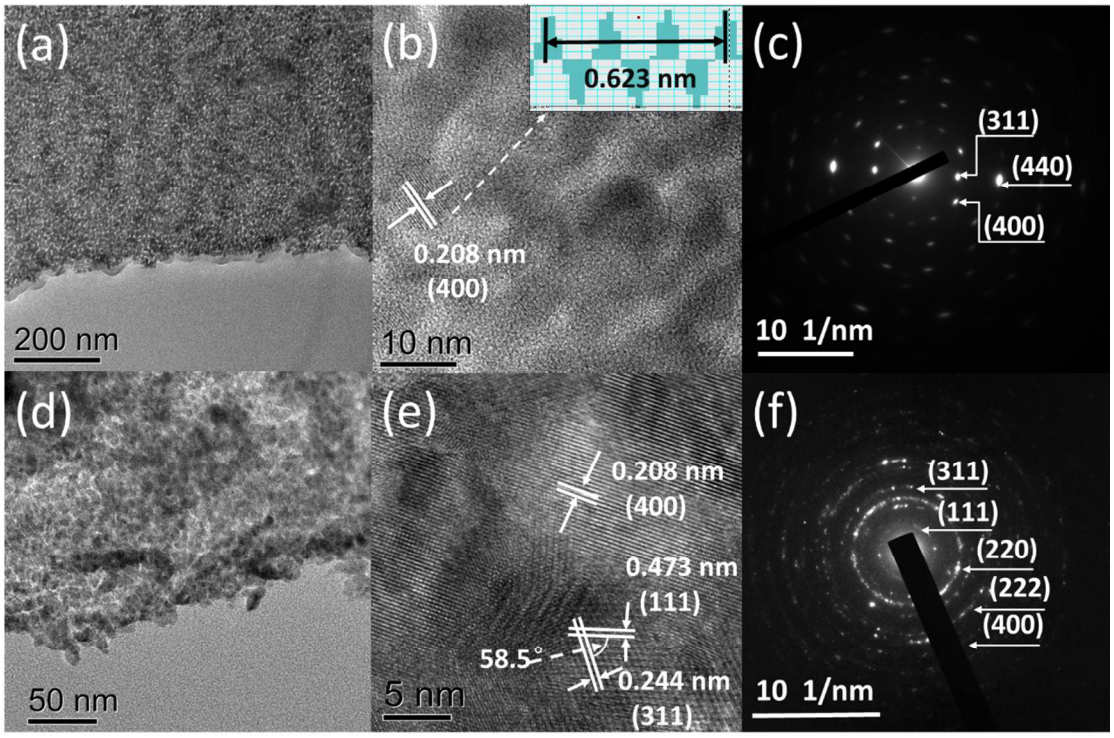


Fig. 4 (a) Structure of $CuCo_2O_4$ nanosheets, low-magnification transmission electron microscopy (TEM) image; (b) high-resolution TEM (HRTEM) image; (c) selected area electron diffraction (SAED) pattern; (d) structure of $MnCo_2O_4$ nanosheets, low-magnification TEM image; (e) HRTEM image; (f) SAED pattern.

Fig. 5

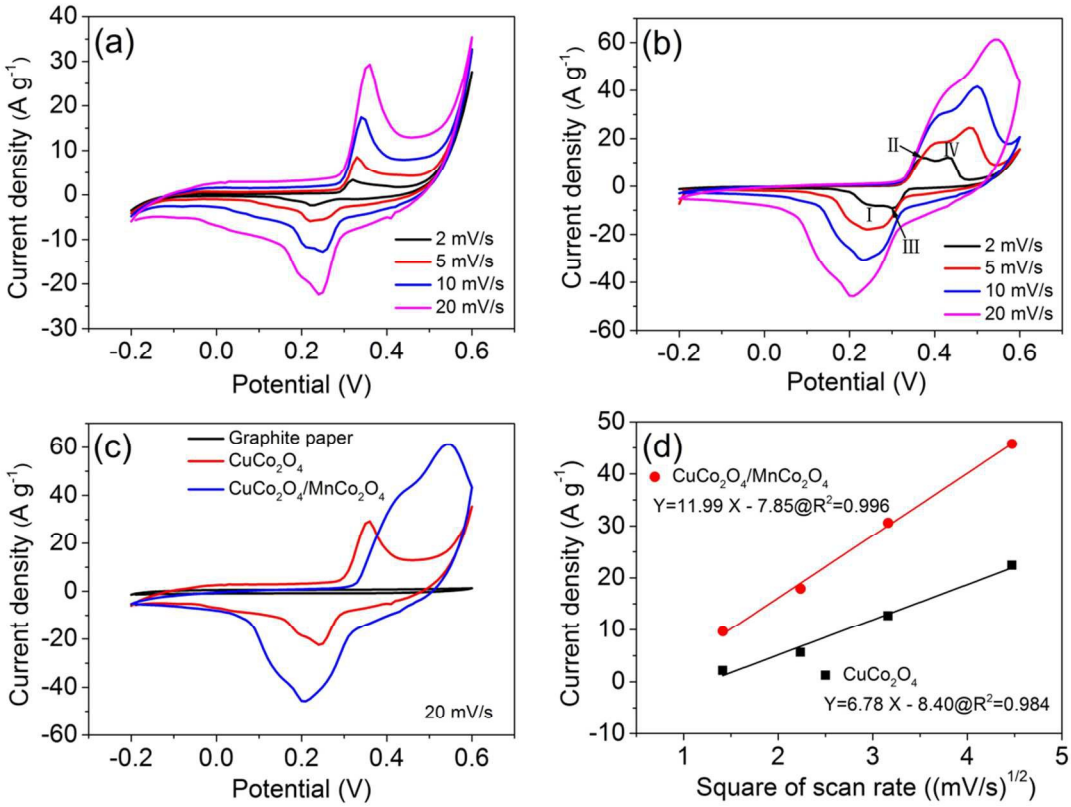


Fig. 5 Cyclic voltammetry (CV) curves of (a) microsphere-like $CuCo_2O_4$ nanosheets and (b) vertically stacked bilayer $CuCo_2O_4/MnCo_2O_4$ heterostructures measured in 2.0 M KOH at various scan rates (2–20 mV $s^{-1}$). (c) CV curves of graphite paper, $CuCo_2O_4$ nanosheets, and $CuCo_2O_4/MnCo_2O_4$ heterostructures at a scan rate of 20 mV $s^{-1}$. (d) Linear relationship between the cathodic peak current and square root of the scan rate of $CuCo_2O_4/MnCo_2O_4$ heterostructures.

Fig. 6

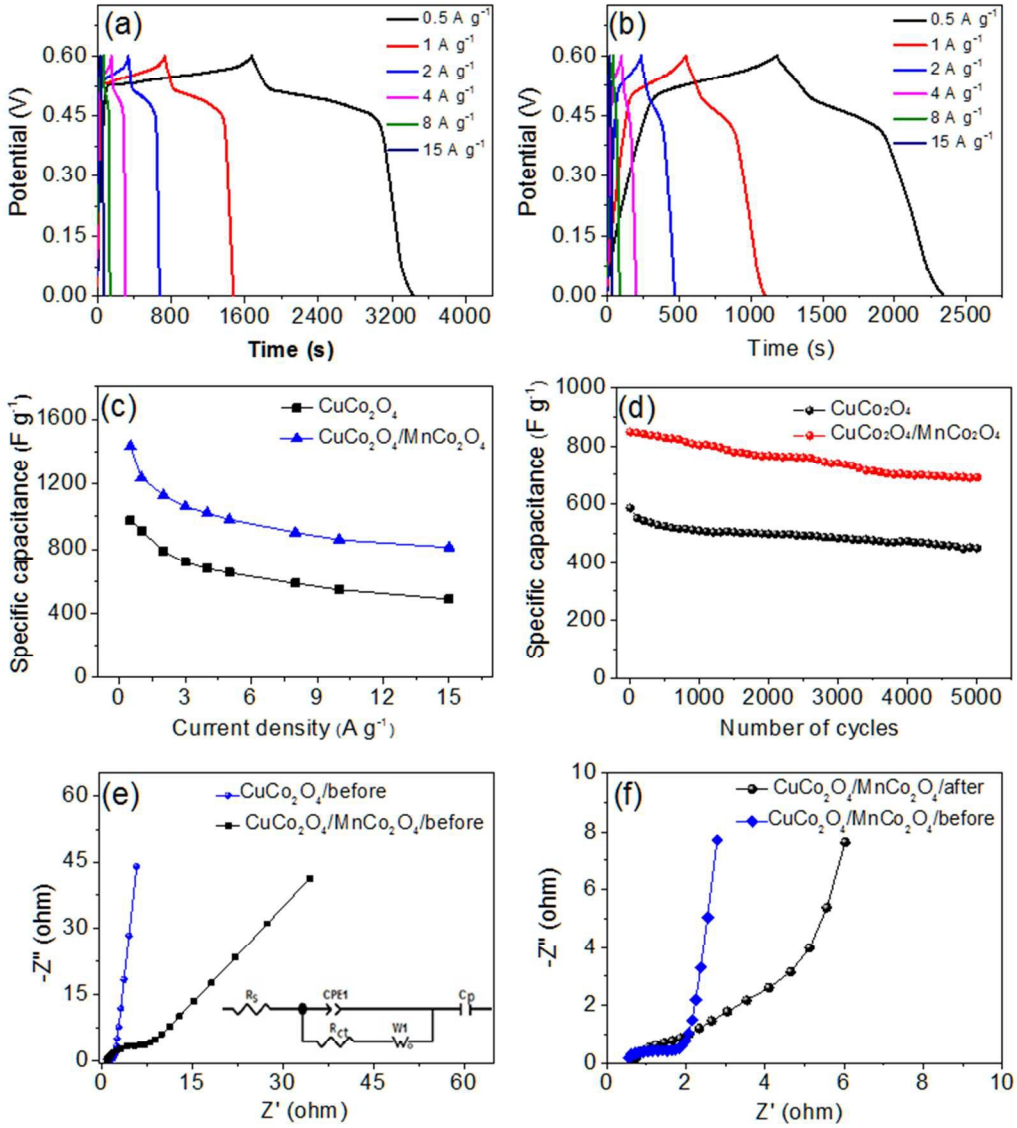


Fig. 6 Galvanostatic charge/discharge curves of (a) $CuCo_2O_4$ and $CuCo_2O_4/MnCo_2O_4$ electrodes at a current density of 0.5 A $g^{-1}$. (b) $CuCo_2O_4/MnCo_2O_4$ electrode measured in a 2.0 M KOH at various current densities (0.5–15 A $g^{-1}$). (c) Specific capacitances of $CuCo_2O_4$ and $CuCo_2O_4/MnCo_2O_4$ electrodes measured at various current densities ranging from 0.5 A $g^{-1}$ to 15 A $g^{-1}$. (d) Cycling performance of $CuCo_2O_4$ and $CuCo_2O_4/MnCo_2O_4$ electrodes at 10 A $g^{-1}$. Electrochemical impedance spectroscopy spectra of (e) $CuCo_2O_4$ and $CuCo_2O_4/MnCo_2O_4$ electrodes (inset: fitted equvialent circuit), and (f) $CuCo_2O_4/MnCo_2O_4$ electrode before and after cycle tests.

Fig. 7

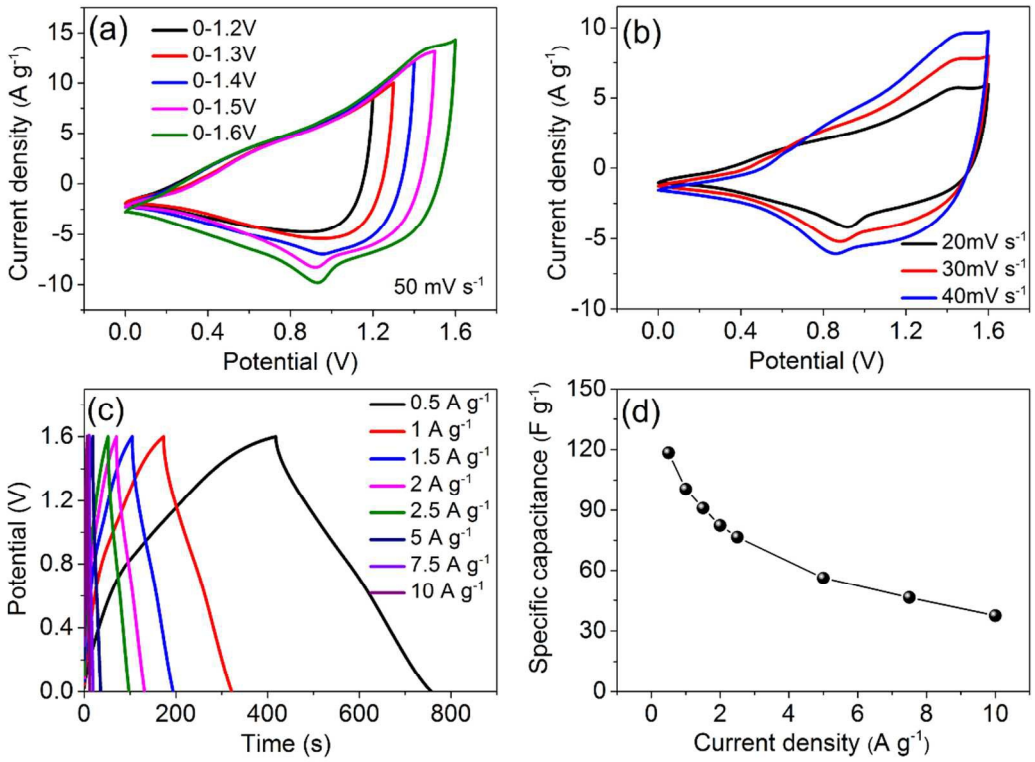


Fig. 7 CV curves of (a) $CuCo_2O_4/MnCo_2O_4$//graphene/NF electrochemical capacitor at different voltage windows and (b) scan rates. (c) Galvanostatic charge/discharge curves and (d) specific capacitances of electrochemical capacitor at different current densities.

Fig. 8

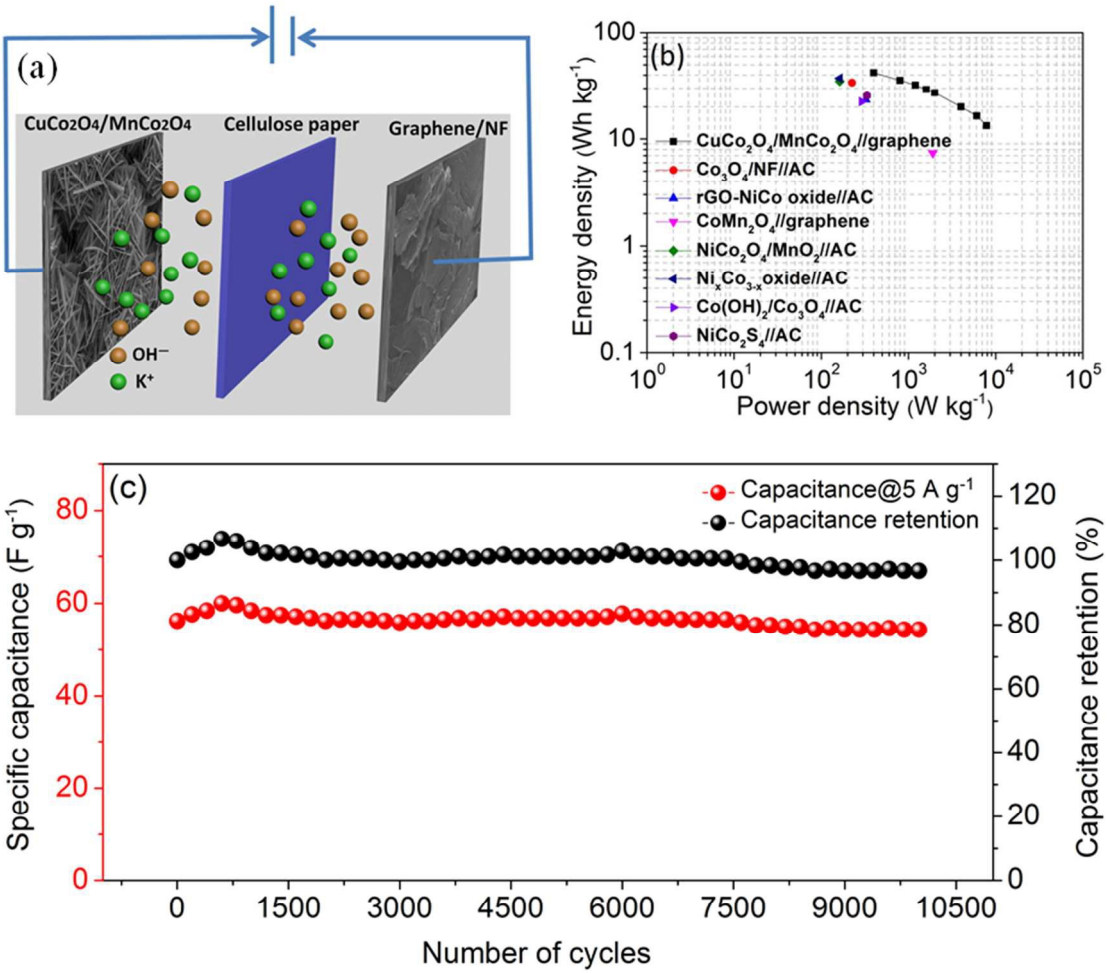


Fig. 8 (a) Schematic of the electrochemical capacitor configuration. (b) Ragone plot of the estimated energy and power densities at different current densities for the hybrid device. (c) Cycling stability of the $CuCo_2O_4/MnCo_2O_4$//graphene/NF hybrid device.

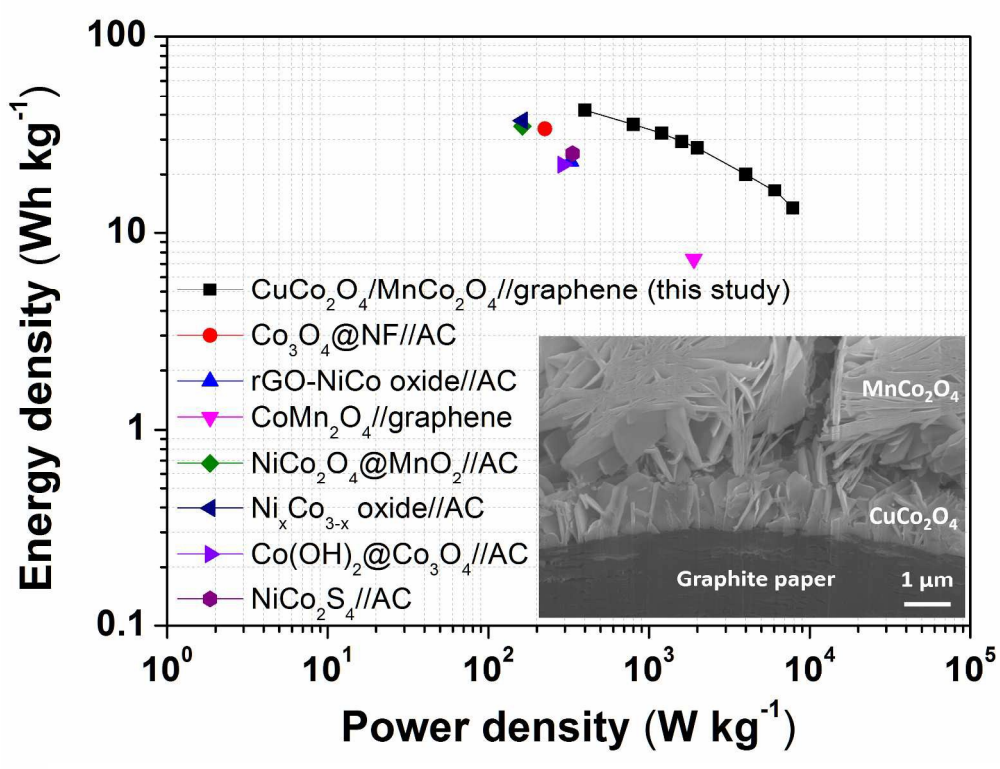


245x188mm (300 x 300 DPI)